Physics of Plasmas ARTICLE scitation.org/journal/php

Linear simulation of kinetic electromagnetic instabilities in a tokamak plasma with weak magnetic shear

Cite as: Phys. Plasmas **28**, 012107 (2021); doi: 10.1063/5.0021362
Submitted: 10 July 2020 · Accepted: 21 December 2020 ·
Published Online: 29 January 2021

Yunchuan Zhao,[1] Jiaqi Wang,[1] Dongjian Liu,[1,a)] Wei Chen,[2] Ge Dong,[3] and Zhihong Lin[4]

AFFILIATIONS

[1]College of Physics, Sichuan University, Chengdu 610065, China
[2]Southwestern Institute of Physics, P.O. Box 432, Chengdu 610041, China
[3]Department of Astrophysical Sciences and Princeton Plasma Physics Laboratory, Princeton, New Jersey 08543, USA
[4]Department of Physics and Astronomy, University of California, Irvine, California 92697, USA

[a)]**Author to whom correspondence should be addressed:** dongjian.liu@gmail.com

ABSTRACT

Gyrokinetic simulation and eigenvalue calculation of electromagnetic instabilities are carried out for an experimentally observed low-n mode in weak magnetic shear discharge. With different magnetic shear values, the Gyrokinetic Toroidal Code simulation of the ion temperature gradient mode is consistent with the eigenvalue code (HD7) calculation. Due to the sensitivity of the kinetic ballooning mode (KBM) to global equilibrium, the simulation of the KBM deviates from the eigenvalue results, for the ballooning representation used in HD7 satisfies its spatial scale separations. Under a flat safety factor profile, the KBM is more unstable and its mode structure tends to move with the peak of the ion temperature drive. Further simulation of the KBM in an HL-2A-like equilibrium shows that the β excitation threshold of the mode is lower than 0.2% and the dominant toroidal mode number is $n = 4$, which is consistent with the measured experimental spectrum.

I. INTRODUCTION

The pressure gradient and unfavorable curvature-driven ballooning mode (BM) is very common in magnetized plasmas,[1] and in a tokamak, this mode determines the critical β (ratio of thermal pressure to magnetic pressure) of plasmas.[2,3] Using an ideal MagnetoHydroDynamics (MHD) model, Dorbrott *et al.*[4] and Coppi[5] obtained a theoretical estimate of the critical β based on high-mode number BM. The properties of ideal BM are modified by kinetic effects (e.g., finite Larmor radii effect, finite orbit width effect, and wave particle interaction). The kinetic BM (KBM) is the kinetic analogue of the ideal MHD BM and has been investigated by Tang *et al.*[6,7] using kinetic MHD ballooning theory, for which the ballooning transformation is employed. For a single poloidal mode localized around the mode rational surface and whose perpendicular wavelength is much shorter than its parallel wavelength, i.e., $k_{\parallel} \ll k_{\perp}$, the width of the mode envelope is determined by the pressure drive, which is on an equilibrium scale. For instance, the ion temperature gradient (ITG) mode, the trapped electron mode (TEM), and the KBM are all characterized by good scale separation. Based on the above scale separation of these modes, the appropriate eikonal form for such oscillations was introduced for a tokamak, known as the ballooning representation.[8] The ballooning formalism reduces the problem to the first-order eikonal partial differential equation, thereby making it easy to obtain the phase and amplitude of the wave along the characteristic lines in weakly non-uniform systems. The transformation has been used widely in analytical calculations; some numerical codes, such as FULL[9,10] and HD7,[11,12] have been used successfully to analyze the ITG mode[13] and TEM.[14]

The hybrid scenario has been designed for next-generation tokamaks[15–18] and offers the possibility of enhanced stability and improved bootstrap current alignment for steady-state operation with a broad region of weak magnetic shear. The low-n electromagnetic modes that have been observed in HL-2A,[19,20] DIII-D,[21] and JET[22] weak magnetic shear experiments can affect the confinement of plasma in the hybrid scenario. For the observed low-n electromagnetic modes, the theoretical gyrokinetic method with the BM representation is not appropriate in the case of a flat safety factor (q) profile. Because of its electromagnetic properties, rotation in the ion diamagnetic drift direction, and

the frequency lying in a range of KBM, it was suspected to be the KBM.[20]

There has been a great deal of analytical work and simulations of the KBM[23–28] to explain the experimental observations and predict the β limit in future tokamaks. Due to the complicated tokamak geometry and multi-scale effect of the mode, it is still far from being understood the long-time behavior of the mode. The present theories and numerical calculations based on the ballooning representation are not applicable for the case of weak magnetic shear, in which the scale separation of these modes is not valid. In this work, the three-dimensional (3D) GTC[29] is used to study electromagnetic instabilities. The GTC is a particle-in-cell code that naturally includes the kinetic effects of the background plasma. In GTC simulation of low frequency electromagnetic waves, thermal ions are simulated by gyrokinetic equations and electrons are modeled using the fluid–kinetic hybrid electron model.[30,31]

The remainder of this paper is as follows. In Sec. II, the simulation models used in GTC and HD7 are introduced. In Sec. III, the numerical study of the KBM is presented. The KBM growth rate, real frequency, and mode structure are studied in the cyclone base case, and the results are the same as those obtained by Xie *et al.*.[32] How magnetic shear influences the KBM is studied systematically. The simulation results are also compared with those obtained using the HD7 gyrokinetic eigenvalue code under the same local equilibrium parameters. Meanwhile, the KBM-driving mechanism is discussed further by using the temperature and density profiles of independent and separated particles. The KBM is also simulated under an HL-2A-like equilibrium. Finally, in Sec. IV, the present work is summarized and possible future work is discussed.

II. SIMULATION MODEL

The simulation model used in the GTC is a kinetic model in five-dimensional (5D) phase space. The plasma is treated as a set of marker particles interacting with each other through self-consistent electromagnetic fields. The fields adopt 3D spatial grids of a field-aligned mesh, and the motion of the particles is tracked in the magnetic flux coordinates. The gyrokinetic formulation and simulation model are as follows.

The Vlasov equation is derived from the gyrokinetic equation by neglecting the collision effects. For the low-frequency waves in a magnetized plasma, the Vlasov equation is written as

$$\frac{d}{dt}f_\alpha(\mathbf{X},\mu,v_\parallel,t)=\left[\frac{\partial}{\partial t}+\dot{\mathbf{X}}\cdot\nabla+\dot{v}_\parallel\frac{\partial}{\partial v_\parallel}\right]f_\alpha=0, \tag{1}$$

where f_α is distribution function, $\mathbf{X}$ is the gyrocenter position in 3D space, μ is the magnetic moment, and $v_\parallel$ is the parallel velocity, which forms a 5D phase space. The subscript α denotes the particle species. The gyrocenter velocity $\dot{\mathbf{X}}$ and the parallel acceleration $\dot{v}_\parallel$ are written as

$$\dot{\mathbf{X}}=v_\parallel\frac{\mathbf{B}}{\mathrm{B_0}}+\mathbf{v}_\mathrm{E}+\mathbf{v}_\mathrm{d}, \tag{2}$$

$$\dot{v}_\parallel=-\frac{1}{\mathrm{m}_\alpha}\frac{\mathbf{B}^*}{\mathrm{B_0}}\cdot(\mu\nabla\mathrm{B_0}+\mathrm{Z}_\alpha\nabla\langle\phi\rangle)-\frac{\mathrm{Z}_\alpha}{\mathrm{m}_\alpha\mathrm{c}}\frac{\partial\langle\mathbf{A}_\parallel\rangle}{\partial\mathrm{t}}, \tag{3}$$

where m_α, Z_α, and c denote the mass, charge of ions, and speed of light. Also, we have $\mathbf{B}\equiv\mathbf{B}_0+\boldsymbol{\delta}\mathbf{B}$, where $\mathbf{B}_0=\mathrm{B_0}\mathbf{b}_0$ and $\boldsymbol{\delta}\mathbf{B}$ are the equilibrium and perturbed magnetic field and $\mathbf{B}^*=\mathbf{B}_0^*+\boldsymbol{\delta}\mathbf{B}$ is the modified magnetic field, with $\mathbf{B}_0^*=\mathbf{B}_0+\frac{\mathrm{B_0}v_\parallel}{\Omega_\alpha}\nabla\times\mathbf{b}_0$, in which Ω_α is the gyro-frequency. Here, ϕ and $\mathbf{A}_\parallel$ are the electrostatic potential and the parallel components of the magnetic vector potential, respectively, and the $B_\parallel$ effect[28,33] is neglected in low β plasmas. $\mathbf{v}_\mathrm{E}$ is the $\mathbf{E}\times\mathbf{B}$ drift, and $\mathbf{v}_d$ is the magnetic drift. Furthermore, $\langle\cdots\rangle\equiv\int\frac{\mathrm{dv_\perp}}{2\pi}d\mathbf{x}\delta(\mathbf{X}+\boldsymbol{\rho}-\mathbf{x})$ is the gyro-orbit averaging, $\boldsymbol{\rho}$ is the gyro-radius, and $\mathbf{x}$ is the position of the particle in 3D coordinates. In Eq. (3), the gyro-Poisson equation and Ampère's law are needed to solve the electrostatic potential ϕ and magnetic vector potential $\mathbf{A}_\parallel$. We define $f=f_0+\delta f$, where f_0 and δf are the equilibrium and perturbed distribution function. Integrating δf, neglecting high order term, and applying Eq. (1), the electron continuity equation is

$$\begin{aligned}&\frac{\partial}{\partial t}\delta n_e+B_0b_0\cdot\nabla\left(\frac{n_{0e}u_{\parallel 0e}}{B_0}\right)+B_0V_E\cdot\nabla\left(\frac{n_{0e}}{B_0}\right)\\&-n_{0e}(v_{*e}+V_E)\cdot\frac{\nabla B_0}{B_0}+\delta B\cdot\nabla\left(\frac{n_{0e}u_{\parallel 0e}}{B_0}\right)\\&+\frac{c\nabla\times B_0}{B_0^2}\cdot\left[-\frac{\nabla\delta P_{\parallel e}}{e}-\frac{(\delta P_{\perp e}-\delta P_{\parallel e})\nabla B_0}{eB_0}+n_{0e}\nabla\Phi\right]=0.\end{aligned} \tag{4}$$

Here, δn_e and $u_{\parallel 0e}$ represent the perturbed electron density and parallel velocity, v_{*e} is the diamagnetic drift velocity, $\delta P_{\parallel e}$ and $\delta P_{\perp e}$ show the perturbed pressure, and all the other symbols have their usual meanings and are mentioned in this paper. The δf simulation[34–36] is used to reduce the discrete particle noise. The fluid kinetic hybrid electron model is adopted, which is built upon the expansion of the electron response into the lowest-order adiabatic part and a higher-order kinetic response, based on the electron–ion mass ratio as a small parameter, in the simulation of electron dynamics. This model is a highly efficient electron model for kinetic simulations of electromagnetic turbulence in the absence of tearing modes.[37] In KBM simulation, where the thermal ion kinetic effect is important, the gyrokinetic ion model is applied in this simulation. Herein, since the physics behavior of KBM is decided by the thermal ions, we neglect the contribution of kinetic electrons and consider the adiabatic electron response for dynamics of low-frequency electromagnetic modes.

The effective potential is defined as $\delta\mathrm{E}_\parallel=-\mathbf{b}_0\cdot\nabla\phi_\mathrm{eff}$. In the kinetic approximation, the adiabatic electron response equation is

$$v_\parallel\mathbf{b}_0\cdot\nabla\delta f_\mathrm{e}=-v_\parallel\frac{\delta\mathbf{B}}{\mathrm{B_0}}\cdot\nabla f_{0\mathrm{e}}-v_\parallel\frac{\delta\mathbf{B}}{\mathrm{B_0}}\cdot\frac{\mu f_{0\mathrm{e}}\nabla\mathrm{B_0}}{T_\mathrm{e}}+v_\parallel\frac{ef_{0e}}{T_\mathrm{e}}\mathbf{b}_0\cdot\nabla\phi_\mathrm{eff}. \tag{5}$$

The adiabatic electron response can be obtained with the Clebsch toroidal magnetic field representation, namely,

$$\delta f_\mathrm{e}=\frac{\mathrm{e}f_{0\mathrm{e}}}{T_\mathrm{e}}\phi_\mathrm{eff}+\left.\frac{\partial f_{0e}}{\partial\psi_0}\right|_{\mathrm{v}_\perp}\delta\psi+\left.\frac{\partial f_{0\mathrm{e}}}{\partial\alpha_0}\right|_{\mathrm{v}_\perp}\delta\alpha, \tag{6}$$

where ψ is the poloidal magnetic flux and $\alpha=q(\psi)\theta-\varsigma$ is the magnetic field line label in terms of the poloidal angle θ and toroidal angle ς in the magnetic flux coordinate. Integrating Eq. (6) in phase space, the lowest order effective potential ϕ_eff is derived as

$$\frac{e\phi_\mathrm{eff}}{T_e}=\frac{\delta\mathrm{n}_e}{\mathrm{n}_{0e}}-\frac{\delta\psi}{\mathrm{n}_{0e}}\frac{\partial\mathrm{n}_{0e}}{\partial\psi_0}-\frac{\delta\alpha}{\mathrm{n}_{0e}}\frac{\partial\mathrm{n}_{0e}}{\partial\alpha_0}. \tag{7}$$

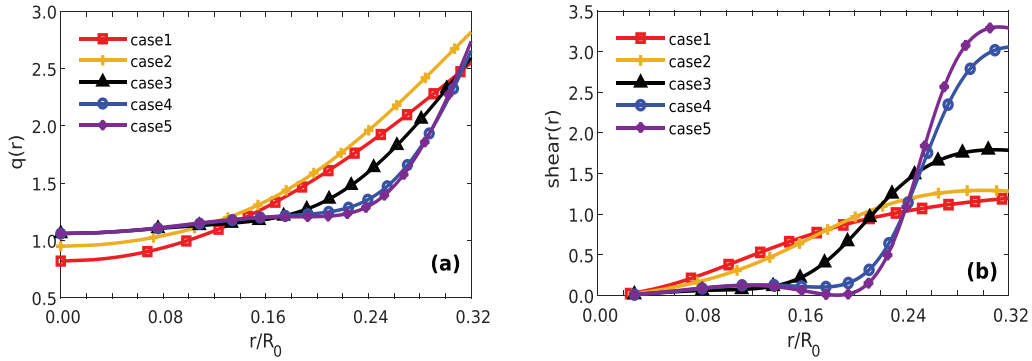

FIG. 1. (a) Different equilibrium q profiles. (b) Corresponding magnetic shear profiles. Here, r is normalized to the major radii R_0, and $R_0 = 167$ cm.

Together with the electron continuity equation and ideal Ohm's law, we have an adiabatic simulation model for electron. More precise kinetic electron effects are described in Ref. 31.

To consider the toroidal coupling effect of high n mode, the ballooning representation is employed in HD7 code. In ballooning angle θ space, the gyrokinetic equation is

$$i\frac{v_\parallel}{Rq}\frac{\partial}{\partial\theta}h_\alpha + (\omega-\omega_{D\alpha})h_\alpha = (\omega-\omega_{*\alpha T})J_0(\delta_\alpha)F_{M\alpha}\frac{q_\alpha n_0}{T_\alpha} \times\left(\hat{\phi}(\theta)-\frac{v_\parallel}{c}\hat{A}_\parallel(\theta)\right). \quad (8)$$

The non-adiabatic response h_α is determined using Eq. (8), in which $\omega_{D\alpha} = 2\epsilon_n\omega_{*\alpha}[\cos\theta + \sin\theta(\hat{s}\theta - \alpha\sin\theta)]\left(\frac{\hat{v}_\perp^2}{2}+\hat{v}_\parallel^2\right)$, $\omega_{*\alpha T} = \omega_{*\alpha}[1+\eta_\alpha\left(\frac{v^2}{v_{t\alpha}^2}-\frac{3}{2}\right)]$, $\delta_\alpha = (2b_\alpha)^{1/2}v_\perp$, $2b_\alpha = k_\perp^2 v_{t\alpha}^2/\Omega_\alpha^2$, $v_{t\alpha}^2 = 2T_\alpha/m_\alpha$, $\omega_{*\alpha} = ck_\theta T_\alpha/q_\alpha BL_n$, and $\Omega_\alpha = q_\alpha B/m_\alpha c$. The symbols represent their usual meanings, such as $\omega_{*\alpha}$ and Ω_α are the diamagnetic drift frequency and the gyrofrequency, respectively. Coupled to the gyro-Poisson equation and Ampère's law, HD7 code solves the integral eigenvalue equation numerically, the code has been successfully used in solving ITG, impurity mode, and one can see Refs. 12 and 13 for more details.

III. NUMERICAL RESULTS

A. GTC simulation of KBM

To study the magnetic shear effects on the KBM, we use the fourth order polynomial function, $q_\psi = a_1 + a_2\cdot(\psi/\psi_w) + a_3\cdot(\psi/\psi_w)^2 + a_4\cdot(\psi/\psi_w)^3 + a_5\cdot(\psi/\psi_w)^4$, as an equilibrium q profile, where "a" represents the adjustable coefficient, ψ shows the poloidal magnetic flux, ψ_w is the poloidal magnetic flux at wall, $\psi_w = 0.0375R_0B_0$, in which R_0 and B_0 are the major radius and on-axis magnetic field, and q_r is the normalized radial coordinate in GTC simulation. Using different coefficients "a," the safety factor (q) profiles in Fig. 1(a) are constructed with the various magnetic shear ($s = rq'/q$) profiles in Fig. 1(b). Here, the five cases are employed and each case shows a specific magnetic shear profile of corresponding safety, as shown in Table I. For the cyclone base case,[38] the parameters are $R_0 = 167$ cm, $R_0/L_T = 6.9$, $R_0/L_n = 2.2$, $T_e = T_i$, $a/R_0 = 0.36$, and $\beta = 2\%$, where R_0, a, L_T, L_n, and β are the tokamak major and minor radii, temperature density gradient scale lengths, and plasma beta, respectively. The KBM growth rate and real frequency are measured for the most unstable mode at the $q = 1.2$ flux surface. The mode number scan with different magnetic shears is presented in Fig. 2. In Fig. 1(a), with different q profiles and cyclone case parameters, the red q profile (i.e., q1) recovers the result in Fig. 2 of Ref. 32.

Figure 2(a) shows that with various magnetic shears, the KBM growth rate first increases and then decreases with the increasing mode number, and the most unstable mode number is approximately 0.22. All the curves in Figs. 2(a) indicate that the growth rate of the KBM saturates with increasing n and a critical value for n should exist. ($k_\theta = m/r$, here, m represents the poloidal mode number and r shows the poloidal radius.) This is probably because that diamagnetic frequency increases linearly with the toroidal mode number, $\omega_{*i} = ck_\theta T_i/QBL_{ni}$, and the diamagnetic effect becomes stronger with the toroidal mode number increasing.[39] More discussions about the diamagnetic effect are discussed in Refs. 40 and 41. Besides, the KBM can be destabilized with decreasing magnetic shear. The blue and purple lines almost coincide when the magnetic shear is lower than 0.11. Thus, magnetic shear has a stabilizing effect on the KBM. Figure 2(b) shows that the simulated real frequency depends linearly on the mode number. In conclusion, the magnetic shear does not influence the real frequency. Figure 3 shows the characteristics of the two-dimensional (2D) mode structure of the most unstable mode ($n = 10$) for different magnetic shears. Figure 3(a) exhibits the mode structure of $\delta\phi$, due to the toroidal geometry effect, the different poloidal mode harmonics couple each other, and it mostly exists in the bad curvature region. Figure 3(b) shows the poloidal harmonics of $\delta\phi$ in the minor radius direction, which are located on the corresponding rational surface.

TABLE I. The different cases of a magnetic shear profile of the corresponding safety factor.

Case	Safety factor	Magnetic shear profile	Local magnetic shear value
Case 1	q_1	s_1	$s = 0.66$
Case 2	q_2	s_2	$s = 0.47$
Case 3	q_3	s_3	$s = 0.31$
Case 4	q_4	s_4	$s = 0.11$
Case 5	q_5	s_5	$s = 0.03$

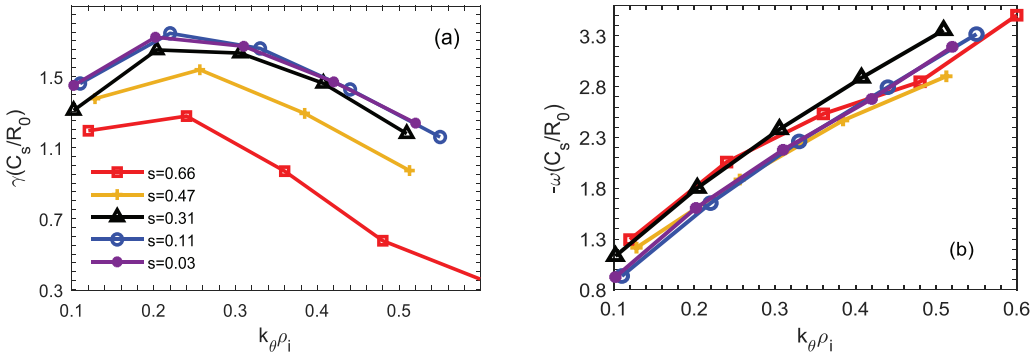

FIG. 2. Kinetic ballooning mode (KBM) growth rate γ (a) and real frequency ω (b) vs $k_\theta\rho_i$ with various magnetic shears.

Figures 3(c) and 3(d) display the mode structure and poloidal harmonics of $\delta\phi$ with weak magnetic shear, respectively. In Figs. 3(b) and 3(d), the pink line represents the q profile and the black dashed line shows the rational surface. Figures 4(b) and 4(d) are as Figs. 3(b) and 3(d). Compared to Figs. 3(a) and 3(b), the only difference in Figs. 3(c) and 3(d) is that the q profile is flat. In cases of flat q (i.e., low magnetic shear), there are few dominant m modes and the mode structure is wider; this is due to the weaker magnetic confinement in cases of lower magnetic shear.

With the purpose of studying the KBM-driving mechanism, we use two hyperbolic tangent functions to fit the ion temperature and density profiles. The peaks of the density and temperature gradients

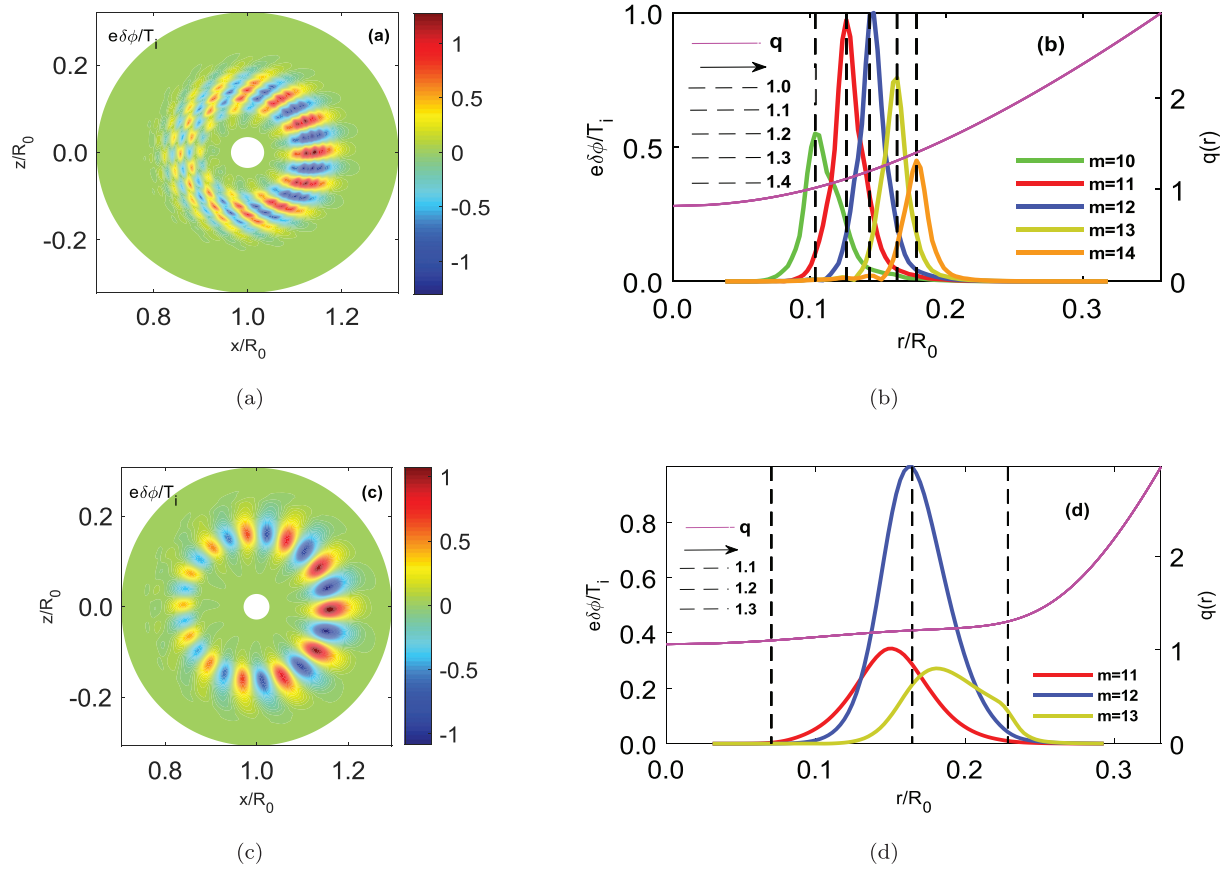

FIG. 3. Two-dimensional mode structure of KBM with the cyclone case parameter: (a) mode structure of $\delta\phi$; (b) poloidal harmonic modes of $\delta\phi$; (c) and (d) $\delta\phi$ and its poloidal harmonics modes with weak magnetic shear. In (b) and (d), the pink line represents the q profile, and the black dashed line shows the rational surface; the same pertains to Figs. 4(b) and 4(d).

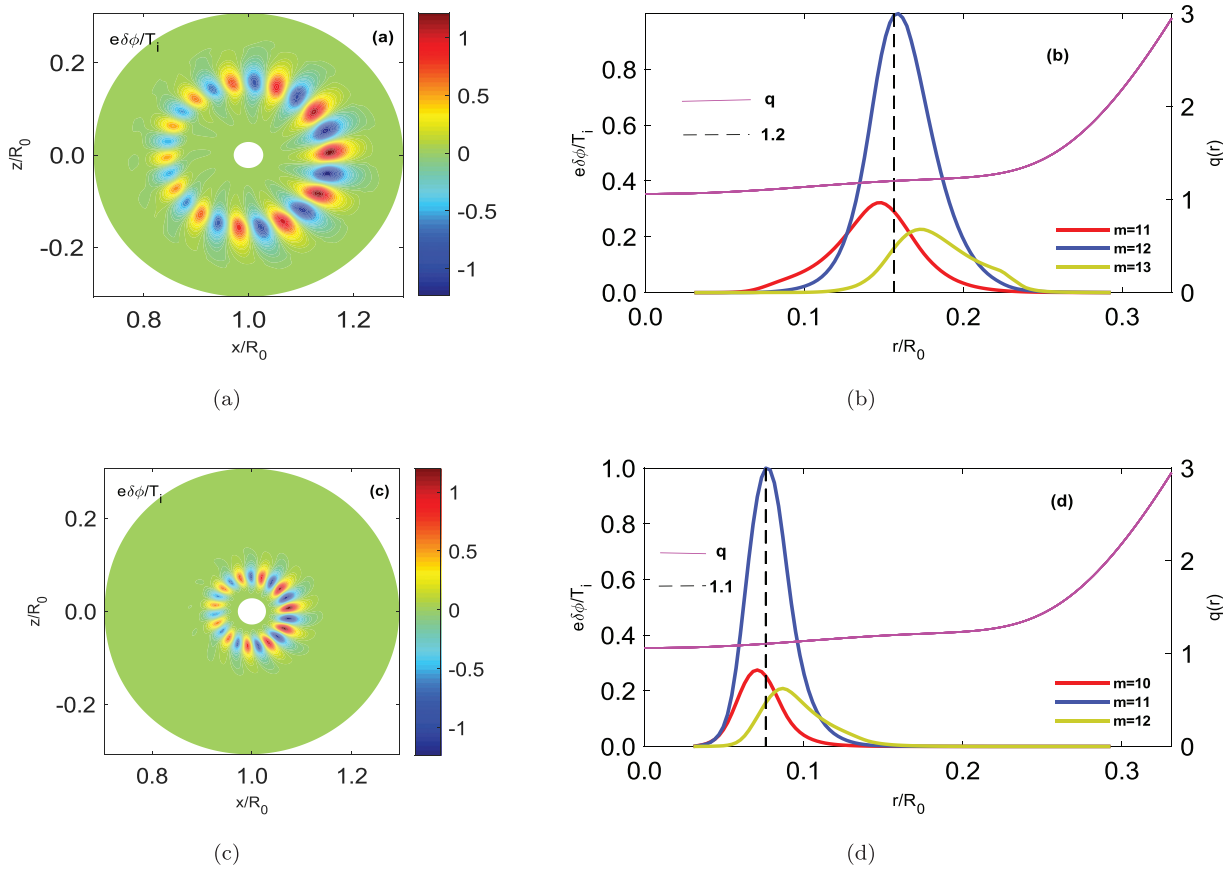

FIG. 4. Two-dimensional mode structure of KBM with weak magnetic shear: (a) and (b) are obtained by moving the peak of the density gradient from the $q = 1.2$ rational surface to the $q = 1.1$ rational surface; (c) and (d) are obtained by moving the peak of the temperature gradient from the $q = 1.2$ rational surface to the $q = 1.1$ rational surface.

are adjusted from the $q = 1.2$ to $q = 1.1$ rational surface separately with the q3 profile in Fig. 1(a). The most unstable toroidal mode number is still $n = 10$ with the same growth rate. The characteristics of the mode structure are shown in Fig. 4, where the mode structure in Figs. 4(a) and 4(b) remains unchanged as the peak of the density gradient moves from the $q = 1.2$ to $q = 1.1$ rational surface. However, Figs. 4(c) and 4(d) show clearly that the KBM structure moves to the $q = 1.1$ surface as the peak of the temperature gradient moves to that surface. With the separate temperature and density profiles in the simulation, it can be concluded that the KBM structure is sensitive to both the rational surface and the temperature gradient.

B. Benchmark between GTC simulation and the HD7 calculation

In this section, for comparison and benchmark purposes, the GTC and HD7 gyrokinetic integral eigenvalue codes are used with the same local parameters to simulate the ITG mode and the KBM. First, the benchmark case of the electrostatic ITG mode is performed with different magnetic shears. Figures 5(a) and 5(b) show the growth rate and real frequency as functions of $k_\theta \rho_i$, and Fig. 5(c) shows the radial mode structure, where the other parameters are $\eta_i = 3.13$, $s = 0.78$, $q = 1.4$, $\epsilon_n = 0.45$, and $\tau = 1$. The most unstable mode number is $k_\theta \rho_i = 0.5$, and the GTC and HD7 results are consistent. With decreasing magnetic shear, Fig. 6 shows similar results: the ITG growth rate increases, while the real frequency remains unchanged. The two codes agree well with each other for the weak magnetic shear case. Thus, the BM representation is always applicable to the ITG mode. Note that the typical ballooning representation requires approximating the spatial scale separation. Here, as given in Table II, we measured the corresponding spatial scale of mode width, distance of the neighboring rational mode surface (RMS), and equilibrium scale from the one-dimensional (1D) radial mode structure and the 1D equilibrium profile of the ITG mode in Figs. 5(c) and 6(c) and the KBM in Figs. 3(b) and 3(d).

As shown in Fig. 7, the veracity of using the HD7 electromagnetic code to study the KBM was assessed using kinetic shear Alfvén (KSA) waves. Figure 7(a) shows the growth rate as a function of $k_\theta \rho_i$, and Fig. 7(b) does the same for the real frequency; the red circles are the results from Fig. 1 of Ref. 12, and black triangles are the HD7 verification results. Thus, KSA benchmarking shows that the HD7 code can be used for electromagnetic studies. However, Fig. 8 shows that the results of KBM using the GTC and HD7 are only qualitatively consistent. As we will see later, the KBM is sensitive to equilibrium:[32] it is

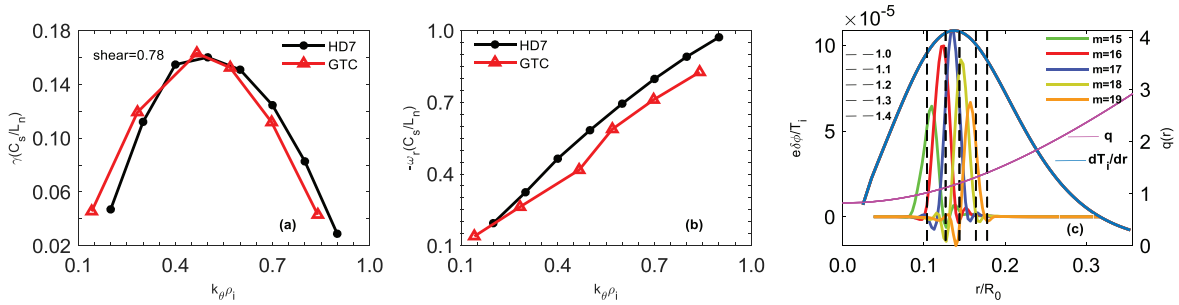

FIG. 5. (a) Growth rate of electrostatic ion temperature gradient (ITG) mode vs $k_\theta \rho_i$. (b) Real frequency vs $k_\theta \rho_i$; the red triangles show the GTC results, and the black circles represent the HD7 results. (c) Radial mode component of $\delta\phi$; the pink line represents the q profile, the black dashed line shows the rational surface, and the light-blue line exhibits the temperature gradient profile.

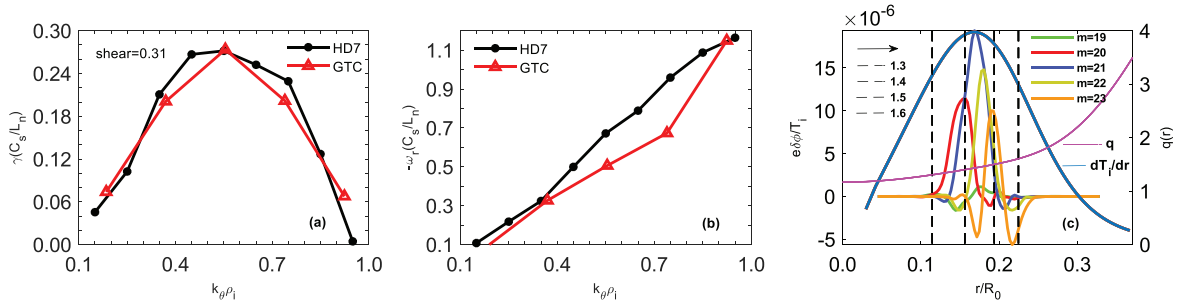

FIG. 6. (a) Growth rate of electrostatic ITG mode vs $k_\theta \rho_i$. (b) Real frequency vs $k_\theta \rho_i$; the red triangles show the GTC results, and the black circles represent the HD7 results. (c) Radial mode component of $\delta\phi$; the other lines are as shown in Fig. 5(c).

TABLE II. Influence of scale separation of ballooning-mode representation on ITG mode and KBM.

Length	Equilibrium scale (R_0)	Distance of nearby RMS (R_0)	Mode width (R_0)
ITG (cyclone case)	10.80Δ	2.25Δ	$\Delta = 0.01490$
ITG ($s = 0.31$)	4.30Δ	2.02Δ	$\Delta = 0.03918$
KBM (cyclone case)	5.89Δ	1.39Δ	$\Delta = 0.02458$
KBM ($s = 0.31$)	4.04Δ	1.83Δ	$\Delta = 0.03993$

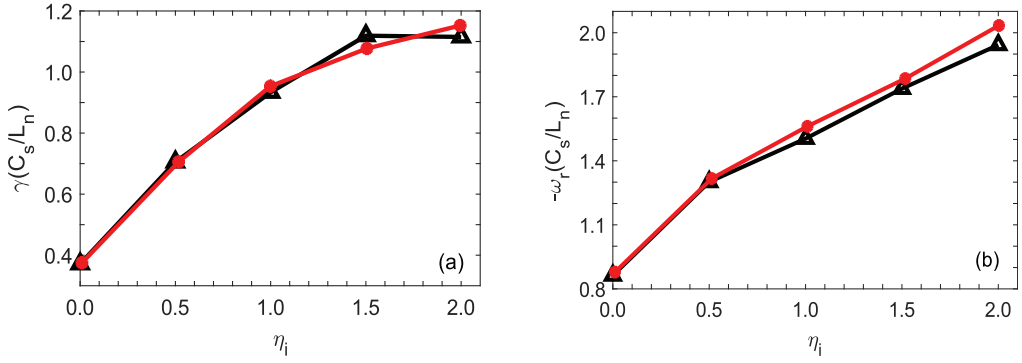

FIG. 7. Verification results for HD7 using kinetic shear Alfvén waves: (a) growth rate vs η_i and (b) real frequency vs η_i. The red circles show the results from Fig. 1 in Ref. 12, and the black triangles represent the HD7 verification results. The other parameters are $k_\theta \rho_s = \sqrt{0.2}$, $s = 0.5$, $\epsilon_n = 0.2$, $\eta_e = 0$, $q = 2.0$, $\tau_i = 1$, and $\beta_i = 0.015$.

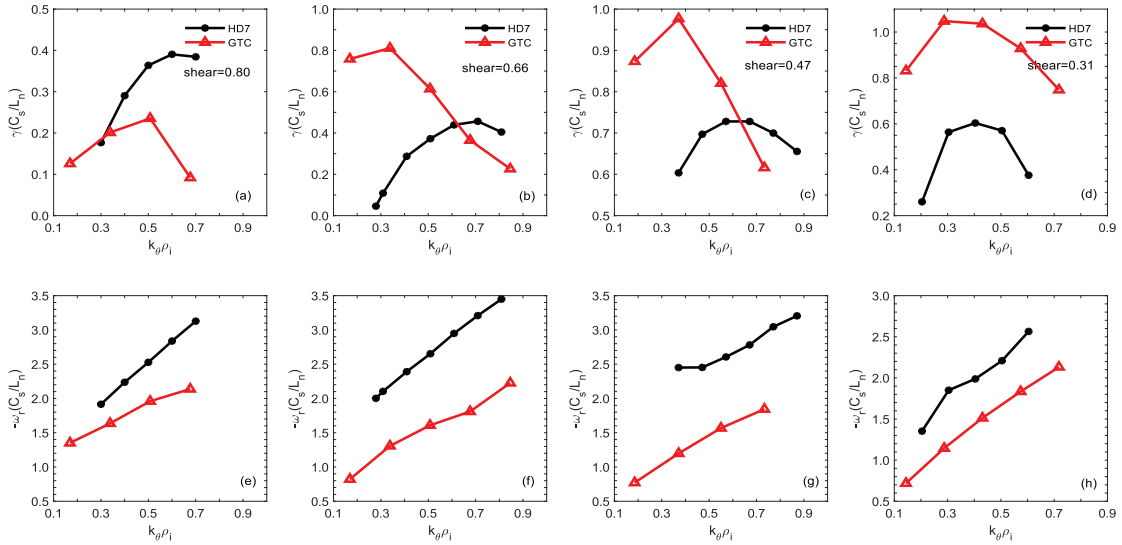

FIG. 8. Growth rate and real frequency vs mode number $k_\theta \rho_i$ with various magnetic shears. The red triangles show the GTC results, and the black circles represent the HD7 results. (a),(b),(c), and (d) are the growth rate, and (e), (f), (g), and (h) are the frequency of KBM vs $k_\theta \rho_i$ with various magnetic shears.

necessary to include the global effect, which is not available in the local HD7 code. From Table II, it is demonstrated that in the cyclone case, the ratio of scale separation is 5.89 : 1.39 : 1; in the magnetic shear = 0.31 case, the ratio of scale separation is 4.04 : 1.83 : 1. Table II shows that the scale separation of the KBM is better when the magnetic shear is 0.31. As shown in Figs. 8(e) and 8(f), the HD7 results approach the GTC ones, where the magnetic shear is relatively low. This may be because the scale separation in the ballooning representation is better in this case. Therefore, it can be concluded that the KBM is sensitive to the global equilibrium (i.e., both the pressure and magnetic profiles).

C. GTC simulation of HL-2A observation

Previously herein, the characteristics of the ITG mode and the KBM were studied in various analytical equilibria with different magnetic shears. In shot 25803 of HL-2A weak magnetic shear experiment, in which R_0 is 165 cm, the inverse aspect ratio is $a/R_0 = 0.24$, on-axis $T_i = 1703$ ev, $n_i = 0.189 \times 10^{14}$ cm^{-3}, and $B_0 = 14\,000$ gauss, the fitted equilibrium profile is shown in Fig. 9, and the local parameters near the q minimum are $T_i \approx 1.1$ keV, $T_e \approx 0.75$ keV, $-R_0 \nabla \ln T_i \approx 32$, $-R_0 \nabla \ln n_i \approx 6$, $\eta_i = \nabla \ln T_i / \nabla \ln n_i \approx 5$, and $s \approx 0$, which are the same as those used in Ref. 20. The instabilities in the experimental observation are detected by Mirnov probes and reveal their electromagnetic character, with the toroidal mode numbers $n = 2 \sim 8$, and these structures propagate in the direction of the ion diamagnetic drift. Figure 10 shows the simulation results. The most unstable toroidal mode number of the KBM decreases to a low number, and the excitation threshold also becomes small. The KBM growth rate increases with the equilibrium current, whereas the real frequency remains almost the same. Thus, the equilibrium current has a destabilizing effect on the KBM with weak magnetic shear.

General KBM theory predicts an excitation threshold of $\beta_e \sim 1.5\%$, with the mode number usually being the high toroidal mode number. However, in this flat q simulation, the low-n KBM can

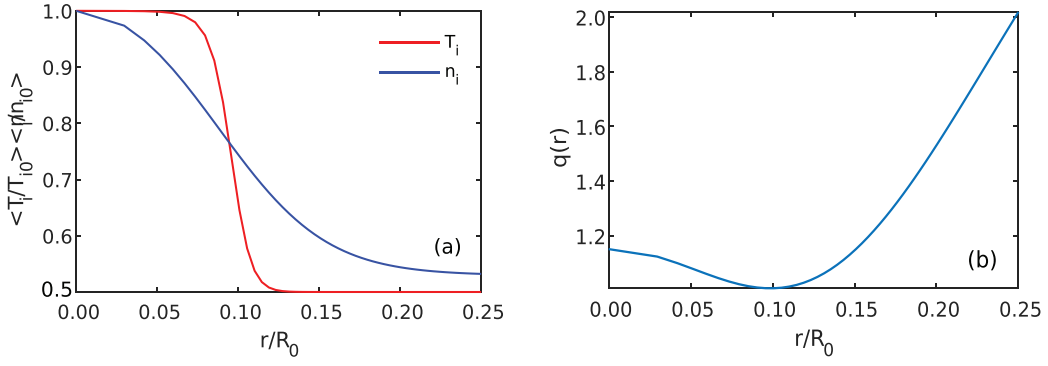

FIG. 9. Equilibrium profiles: (a) ion temperature and density profile; T_i is normalized to $T_{i0} = 1703$ eV; n_i is normalized to $n_{i0} = 0.189 \times 10^{14}$ cm^{-3}; (b) safety factor profile. Here, r is normalized to the major radius, and $R_0 = 165$ cm.

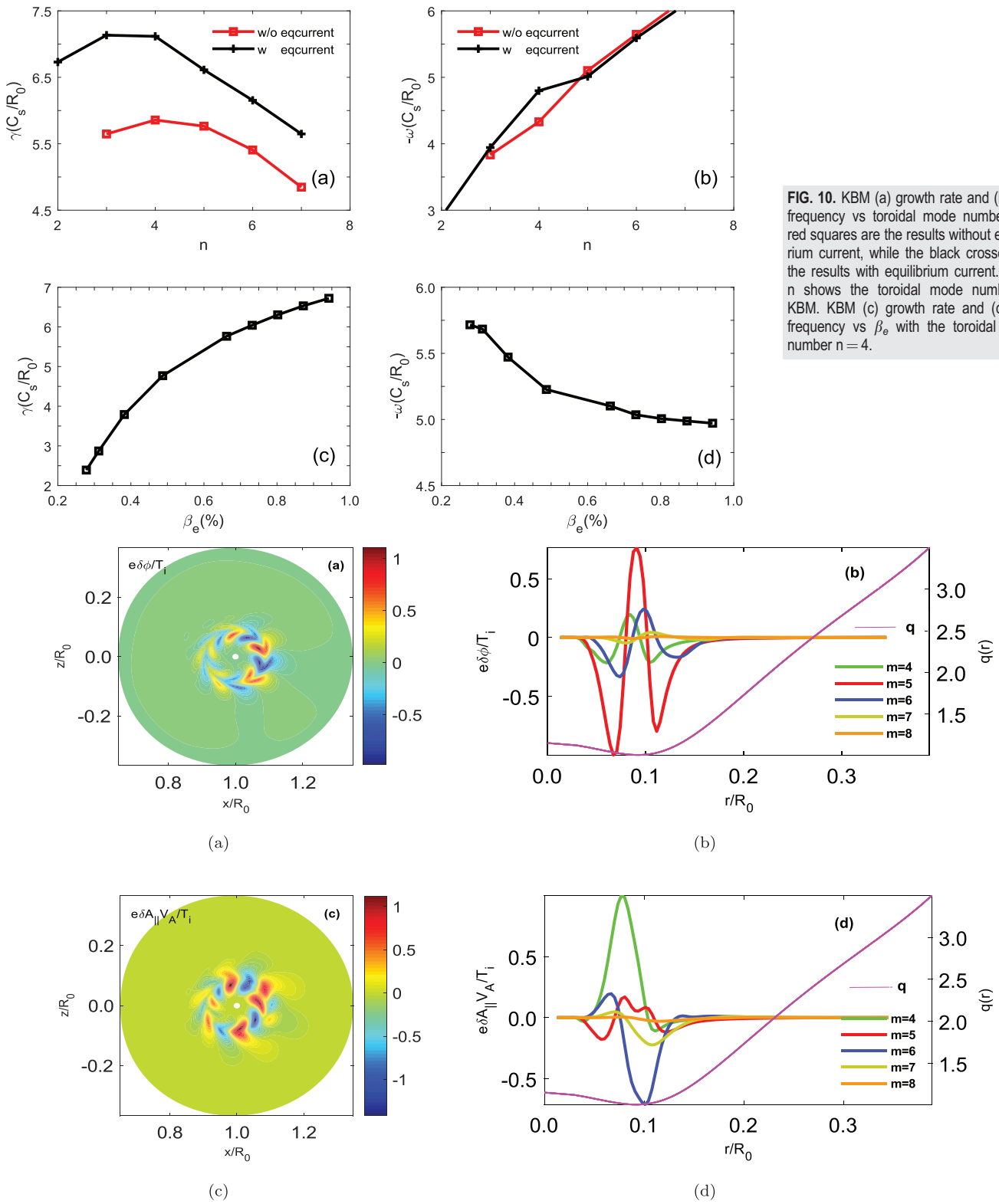

FIG. 10. KBM (a) growth rate and (b) real frequency vs toroidal mode number; the red squares are the results without equilibrium current, while the black crosses are the results with equilibrium current. Here, n shows the toroidal mode number of KBM. KBM (c) growth rate and (d) real frequency vs β_e with the toroidal mode number n = 4.

FIG. 11. Poloidal contours (a) $\delta\phi$ and (c) $\delta A_{||}$ of KBM. Poloidal harmonic modes of (b) $\delta\phi$ and (d) $\delta A_{||}$ of KBM with n = 4; the pink line shows the safety factor profile.

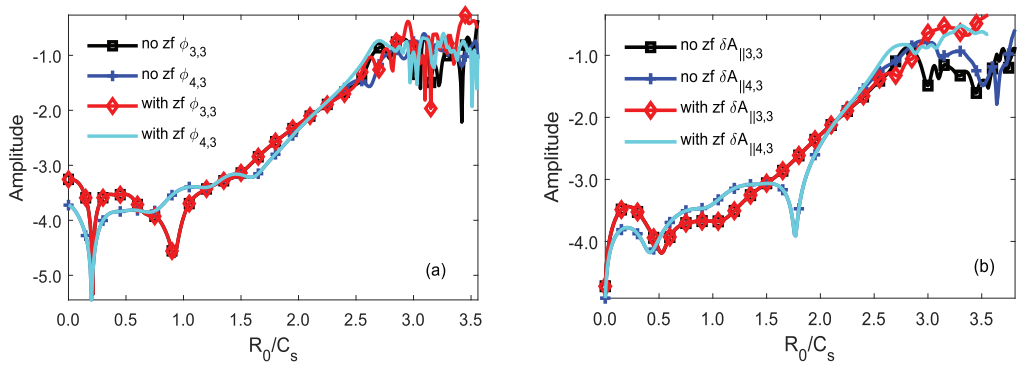

FIG. 12. Time history of the normalized perturbed electrostatic potential ϕ (a) and parallel vector potential $\delta A_{||}$ (b) for the mode (m = 3 and m = 4 and n = 3) measured at the q = 1.0 rational surface in a simulation with or without the self-consistently generated zonal component.

also develop; a lower excitation threshold is needed to destabilize the mode, and the equilibrium current[42] also has a destabilizing effect on the KBM. Here, the β scan in Fig. 10(c) shows that β has a destabilizing effect on the KBM, and in Fig. 10(d), the frequency decreases slightly with increasing β. These results are consistent with the qualitative analysis of the experiment.[20] In the simulation, the low toroidal mode number instability developed, around the magnetic shear, $s \sim 0$, and the experimental β falls into the simulated excitation threshold $\beta \sim 0.2\%$. The magnetic component of the instability is comparable with the electrostatic component. Meanwhile, the real frequency is decided by ion diamagnetic drift frequency. Therefore, the electromagnetic mode is identified to be KBM. Meanwhile, Fig. 11 shows the 2D

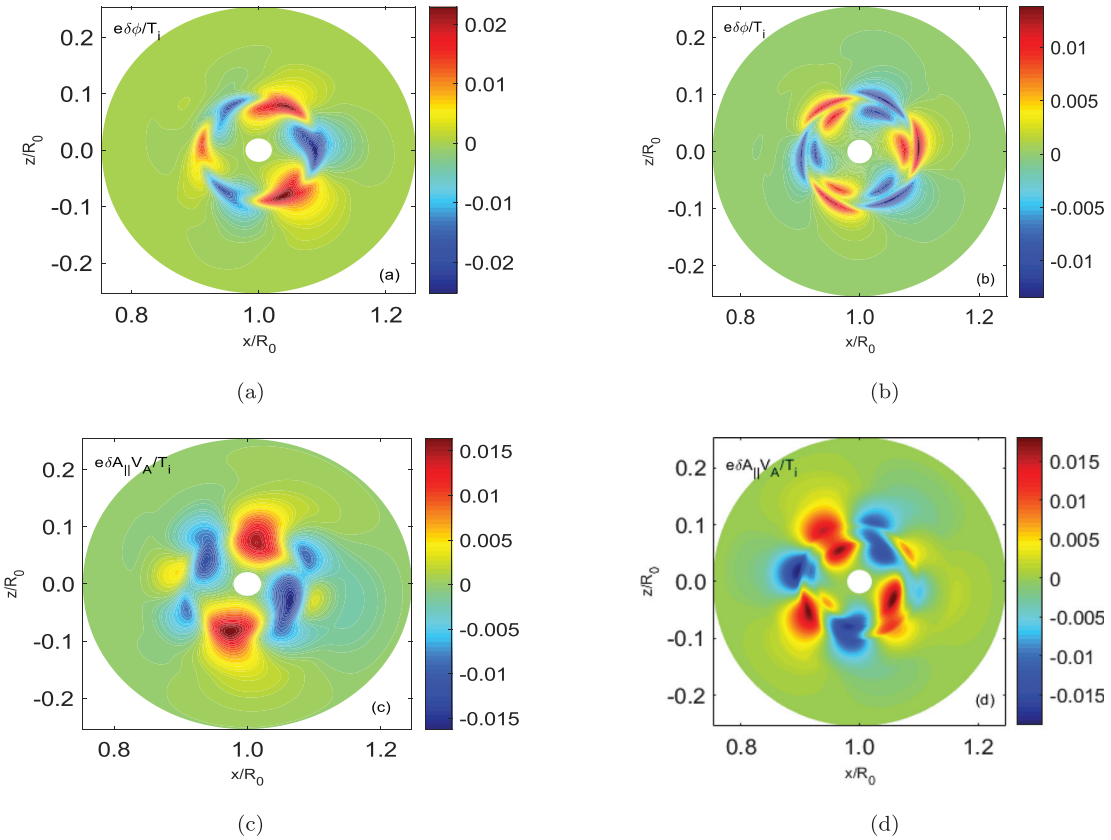

FIG. 13. Poloidal contour of the perturbed electrostatic potential ϕ and perturbed parallel vector potential $\delta A_{||}$ in the nonlinear regime. Panels (a) and (c) show the macroscale radial structure in the simulation with the zonal component artificially suppressed. Panels (b) and (d) show the radial structure in the simulation with the self-consistently generated zonal component.

mode structure; there are a few much wider poloidal harmonics in the radial mode, with these being due to the weak magnetic confinement effect of the flat q profile, which was mentioned in Sec. III. A time history for the nonlinear KBM simulation in shot 25803 of HL-2A weak magnetic shear experiment is shown in Fig. 12. The perturbed parallel vector potential is normalized as $e\delta A_{\parallel} v_A/T_i$, respectively, where $v_A = B_0/\sqrt{4\pi n_0 m_i}$. At $t \sim 1.5R_0/C_s$, $\delta A_{\parallel}$ starts to grow exponentially, which indicates that the mode evolves into an intermediate regime. From $t \sim 1.5R_0/C_s$ to $t \sim 2.7R_0/C_s$, $\delta A_{\parallel}$ grows slightly faster than its linear phase. The $\delta\phi$ mode saturation level without the zonal component is comparable with the zonal component one in Fig. 12(a). As shown in Fig. 12(b), the $\delta A_{\parallel 4,3}$ mode saturation level is slightly higher than $\delta A_{\parallel 3,3}$. In this regime, $\delta\phi$ retains its linear poloidal mode structure. Mode saturation (around $t \sim 3.0R_0/C_s$ in this case) indicates the end of the intermediate regime. In the saturation stage, $\delta A_{\parallel 3,3}$ saturates at a magnitude higher than the case without the zonal current. This indicates that zonal current affects the KBM saturation level. A comparison of the $\delta\phi$ and $\delta A_{||}$ nonlinear poloidal structures between simulations with and without the zonal component is shown in Fig. 13. As shown in Fig. 13(b) (d), the zonal components break the radially elongated eigenmode structure into small scales. It can be concluded that the KBM saturation is influenced by the zonal current.

IV. DISCUSSION AND CONCLUSION

In this paper, the linear properties of electromagnetic instabilities in tokamak plasmas with different magnetic shears have been investigated by both the GTC simulation and the HD7 calculation. For cyclone case equilibrium, the GTC simulation shows that the most unstable toroidal mode number of the KBM is $n = 10$, with various poloidal mode numbers coupled together, and the 2D structure of the mode is the typical BM structure. As to the effect of magnetic shear, it has an obvious stabilizing effect on the KBM: the KBM linear growth rate increases with weaker magnetic shear, while the KBM real frequency, which is determined by the ion diamagnetic drift frequency, remains the same. Compared to strong magnetic shear, the GTC simulation shows that there are few dominant poloidal harmonic modes in weak magnetic shear equilibrium, the radial mode structure is wider, and the envelope of the mode is determined by the dominant mode. Furthermore, the mode structure of the KBM is more sensitive to the ion temperature gradient and tends to move with the drive, which can centralize around the relative mode rational surface.

Comparing the GTC simulation with the HD7 eigenvalue calculation, it is found that the KBM is more sensitive to the equilibrium profile, and the ballooning-representation-based code is sufficient for revealing the ITG properties. However, it is not applicable to analyzing the KBM with weak magnetic shear, even for high toroidal mode numbers, in which the approximation for the ballooning representation is sufficient. Because the KBM is more sensitive to the equilibrium profile, a more general method with full geometry effects is needed for both analytical work and simulation.

In simulation of the HL-2A weak magnetic shear experiment, there is good agreement between the simulation and experimental results with the fitted equilibrium of the HL-2A experiment. The GTC simulation indicates that the dominant toroidal mode number is between 3 and 7, and the excitation threshold of β decreases to 0.2% with weak magnetic shear. The zonal component breaks the radially elongated eigenmode structure into microscale and mesoscale structures. It can be concluded that the KBM with a weak magnetic shear saturation is governed by the zonal fields. To explain the experimental observation and predict the long-time behavior of this mode in the hybrid scenario, a nonlinear KBM simulation will be performed for numerical equilibrium of a realistic tokamak.

ACKNOWLEDGMENTS

This work was supported by the U.S. DOE SciDAC GSEP Center, National MCF Energy R&D Program (Grant No. 2019YFE03060000), the China National Magnetic Confinement Fusion Science Program (Grant Nos. 2013GB112005, and 2015GB110004), the National Natural Science Foundation of China (Grant Nos. 11205109 and 11275162), the Sichuan Science and Technology Program (No. 2017JY0224), and the Innovation Spark Project of Sichuan University (No. Z). This research used resources of the Oak Ridge Leadership Computing Facility at the Oak Ridge National Laboratory (DOE Contract No. DE-AC05–00OR22725) and the National Energy Research Scientific Computing Center (DOE Contract No. DE-AC02–05CH11231).

DATA AVAILABILITY

The data that support the findings of this study are available from the corresponding author upon reasonable request.

REFERENCES

[1]G. Vetoulis and L. Chen, J. Geophys. Res. Space Phys. **101**, 15441, https://doi.org/10.1029/96JA00494 (1996).
[2]J. P. Freidberg, Rev. Mod. Phys. **54**, 801 (1982).
[3]M. S. Chance, S. C. Jardin, and T. H. Stix, Phys. Rev. Lett. **51**, 1963 (1983).
[4]D. Dorbrott, D. B. Nelson, J. M. Greene, A. H. Glasser, M. S. Chance, and E. A. Frieman, Phys. Rev. Lett. **39**, 943 (1977).
[5]B. Coppi, Phys. Rev. Lett. **39**, 939 (1977).
[6]W. M. Tang, J. W. Connor, and R. J. Hastie, Nucl. Fusion **20**, 1439 (1980).
[7]W. M. Tang, G. Rewoldt, C. Z. Cheng, and M. S. Chance, Nucl. Fusion **25**, 151 (1985).
[8]J. W. Connor, R. J. Hastie, and J. B. Taylor, Proc. R. Soc. Lond. A **365**, 1 (1979).
[9]G. Rewoldt, W. M. Tang, and M. S. Chance, Phys. Fluids **25**, 480 (1982).
[10]G. Rewoldt, W. M. Tang, and R. J. Hastie, Phys. Fluids **30**, 807 (1987).
[11]J. Q. Dong, L. Chen, and F. Zonca, Nucl. Fusion **39**, 1041 (1999).
[12]J. Q. Dong, L. Chen, F. Zonca, and G. D. Jian, Phys. Plasmas **11**, 997 (2004).
[13]J. Q. Dong, W. Horton, and J. Y. Kim, Phys. Fluids B **4**, 1867 (1992).
[14]Y. Shen, J. Q. Dong, A. P. Sun, H. P. Qu, G. M. Lu, Z. X. He, H. D. He, and L. F. Wang, Plasma Phys. Controlled Fusion **58**, 045028 (2016).
[15]M. Shimada, D. J. Campbell, V. Mukhovatov, M. Fujiwara, N. Kirneva, K. Lackner, M. Nagami, V. D. Pustovitov, N. Uckan, J. Wesley *et al.*, Nucl. Fusion **47**, S1 (2007).
[16]D. C. McDonald, L. Laborde, J. C. DeBoo, F. Ryter, M. Brix, C. D. Challis, P. de Vries, C. Giroud, J. Hobirk, D. Howell *et al.*, Plasma Phys. Controlled Fusion **50**, 124013 (2008).
[17]C. Gormezano, A. Becoulet, P. Buratti, L. Carraro, F. Crisanti, B. Esposito, G. Giruzzi, R. Guirlet, G. T. Hoang, E. Joffrin *et al.*, Plasma Phys. Controlled Fusion **46**, B435 (2004).
[18]C. Gormezano, A. C. C. Sips, T. C. Luce, S. Ide, A. Becoulet, X. Litaudon, A. Isayama, J. Hobirk, M. R. Wade, T. Oikawa *et al.*, Nucl. Fusion **47**, S285 (2007).
[19]W. Chen, R. R. Ma, Y. Y. Li, Z. B. Shi, H. R. Du, M. Jiang, L. M. Yu, B. S. Yuan, Y. G. Li, Z. C. Yang *et al.*, Europhys. Lett. **116**, 45003 (2016).
[20]W. Chen, D. L. Yu, R. R. Ma, P. W. Shi, Y. Y. Li, Z. B. Shi, H. R. Du, X. Q. Ji, M. Jiang, L. M. Yu *et al.*, Nucl. Fusion **58**, 056004 (2018).
[21]Z. Yan, G. R. McKee, R. J. Groebner, F. B. Snyder, T. H. Osborne, and K. H. Burrell, Phys. Rev. Lett. **107**, 055004 (2011).
[22]S. Moradi, I. Pusztai, I. Voitsekhovitch, L. Garzotti, C. Bourdelle, M. J. Pueschel, I. Lupelli, and M. Romanelli, Nucl. Fusion **54**, 123016 (2014).

[23]C. Z. Cheng, Phys. Fluids **25**, 1020 (1982).
[24]F. Zonca, L. Chen, and R. A. Santoro, Plasma Phys. Controlled Fusion **38**, 2011 (1996).
[25]L. J. Zheng and M. Tessarotto, Phys. Plasmas **1**, 3928 (1994).
[26]H. Qin, W. M. Tang, and G. Rewoldt, Phys. Plasmas **6**, 2544 (1999).
[27]Y. Li and Y. Xiao, Phys. Plasmas **24**, 081202 (2017).
[28]G. Dong, J. Jian, A. Bhattacharjee, A. Brizard, Z. H. Lin, and P. Porazik, Phys. Plasmas **24**, 081205 (2017).
[29]Z. Lin, T. S. Hahm, W. W. Lee, W. M. Tang, and R. B. White, Science **281**, 1835 (1998).
[30]I. Holod and Z. Lin, Phys. Plasmas **20**, 032309 (2013).
[31]Z. Lin and L. Chen, Phys. Plasmas **8**, 1447 (2001).
[32]H. S. Xie, Y. Xiao, I. Holod, Z. Lin, and E. A. Belli, J. Plasma Phys. **82**, 905820503 (2016).
[33]N. Joiner, A. Hirose, and W. Dorland, Phys. Plasmas **17**, 072104 (2010).
[34]A. M. Dimits and W. W. Lee, J. Comput. Phys. **107**, 309 (1993).
[35]S. E. Parker and W. W. Lee, Phys. Fluids B **5**, 77 (1993).
[36]I. Holod, W. L. Zhang, Y. Xiao, and Z. Lin, Phys. Plasmas **16**, 122307 (2009).
[37]D. Liu, J. Bao, T. Han, J. Wang, and Z. Lin, Phys. Plasmas **23**, 022502 (2016).
[38]A. M. Dimits, G. Bateman, M. A. Beer, B. I. Cohen, W. Dorland, G. W. Hammett, C. Kim, J. E. Kinsey, M. Kotschenreuther, A. H. Kritz *et al.*, Phys. Plasmas **7**, 969 (2000).
[39]G. T. A. Huysmans, S. E. Sharapov, A. B. Mikhailovskii, and W. Kerner, Phys. Plasmas **8**, 4292 (2001).
[40]N. Aiba, M. Honda, and K. Kamiya, Nucl. Fusion **57**, 022011 (2017).
[41]W. M. Tang, R. L. Dewar, and J. Manickam, Nucl. Fusion **22**, 1079 (1982).
[42]D. Liu, W. Zhang, M. C. Joseph, J. Wang, and Z. Lin, Phys. Plasmas **21**, 122520 (2014).